Electrochimica Acta 344 (2020) 136174

Contents lists available at ScienceDirect

Electrochimica Acta

journal homepage: www.elsevier.com/locate/electacta

Layered double hydroxides derived NiCo-sulfide as a cathode material for aluminum ion batteries

Wei Xing [a, b, *, 1], Xiaochen Li [a, 1], Tonghui Cai [a, 1], Yu Zhang [a], Peng Bai [a], Jing Xu [a], Han Hu [b], Mingbo Wu [b], Qingzhong Xue [a, b], Yi Zhao [c], Jin Zhou [c], Shuping Zhuo [c], Xiuli Gao [b, **], Zifeng Yan [a]

[a] State Key Laboratory of Heavy Oil Processing, School of Material Science and Engineering, China University of Petroleum, Qingdao, 266580, PR China
[b] Institute of New Energy, China University of Petroleum, Qingdao, 266580, PR China
[c] School of Chemistry and Chemical Engineering, Shandong University of Technology, Zibo, 255049, PR China

ARTICLE INFO

Article history:
Received 20 January 2020
Received in revised form
1 April 2020
Accepted 2 April 2020
Available online 5 April 2020

Keywords:
Aluminum-ion battery
Layered double hydroxide
Metal sulfide
Cathode material
Specific capacity

ABSTRACT

Aluminum-ion batteries (AIBs) is a type of emerging device for large scale energy storage. Developing new and efficient cathode materials is a hotspot in this research area. Herein, a strategy combining the layer double hydroxides (LDHs) synthesis in the presence of graphene oxide (GO) and subsequent sulfidation is developed to prepare a composite of nickel-cobalt sulfides and reduced graphene oxide (rGO). The resulting sulfurized product (S–NiCo@rGO) exhibits a high discharge capacity of 248.2 mA h g^{-1} at the current density of 1 A g^{-1} and maintains a discharge capacity of 83 mA h g^{-1} with nearly 100% coulombic efficiency after 100 cycles. The energy storage mechanism of this material is disclosed to be due to the substitution of Ni^{2+} and Co^{2+}/Co^{3+} by Al^{3+}. The material and the finding obtained in this work are significant for the development of high performance AIBs using LDH-derived materials.

1. Introduction

Nowadays, due to the increasing demand of energy as well as the deteriorating environment problems, affordable and environmentally friendly energy storage devices such as rechargeable batteries have attracted widespread attention. Among current various batteries, lithium-ion batteries (LIBs) are most widely used for electrical energy storage due to their high energy and power density. However, the extensive application of lithium-based rechargeable batteries is restricted by some critical factors in terms of high battery cost and limited lithium resources. Therefore, some new types of rechargeable batteries using the earth abundant element, such as sodium-ion batteries [1–3], magnesium-ion batteries [4–6] and aluminum-ion batteries (AIBs) [7–11], have been considered as prospective alternatives to LIBs.

AIBs have gradually gained extensively attention in consideration of battery cost and security issues. Aluminum is the most abundant metal element in the earth crust. In addition, a three-electron transfer property during redox reactions potentially leads to high capacity and energy density. In the earlier studies, aqueous electrolytes were applied for aluminum batteries due to easy operation and low cost. However, there are two critical reasons hindering the development of Al batteries with aqueous electrolyte system [12–14]. One of them is the formation of a protective oxide film on the surface of aluminum and the other is the easily occurring water splitting on the electrode surface. Both these two characters result in a serious decrease in energy efficiency. To overcome these disadvantages, non-aqueous electrolytes were developed for Al-based batteries.

Over the past few years, many researches were conducted to explore appropriate cathode materials for AIBs employing non-aqueous electrolytes. Dai's group at Stanford University first adopted the graphite foam and aluminum foil as cathode and anode materials, respectively [15]. This combination possesses a discharge capacity of about 60 mA h g^{-1} with high discharge voltage plateau (~2 V), extraordinary cycle stability and high coulombic efficiency. Besides these graphite [16,17] or graphene based materials [18–20],

* Corresponding author. State Key Laboratory of Heavy Oil Processing, School of Material Science and Engineering, China University of Petroleum, Qingdao, 266580, PR China.
** Corresponding author.
E-mail address: xingwei@upc.edu.cn (W. Xing).
[1] Wei Xing, Xiaochen Li and Tonghui Cai contribute equally to this work.

https://doi.org/10.1016/j.electacta.2020.136174
0013-4686/

transition metal sulfides gradually drew attention due to their simple synthesis and low cost. However, most researches focused on monotypic sulfides [10,21–25], which presented poor electrical conductivity and inferior ion diffusion channels within its bulk phase. By contrast, multicomponent sulfides are supposed to be endowed with extraordinary electrical conductivity and better electrochemical activity due to the co-existence of different metal ions [26,27]. In particular, Ni_xCo_yS has been extensively investigated as the electrode materials of batteries [28,29] and supercapacitors [30,31] on account of their unique physical and chemical properties. Nevertheless, the binary nickel cobalt sulfides have not yet been investigated as a cathode material of AIBs.

On the other side, LDHs have gained increasing attention in various aspects, such as catalysis, biotechnology and electrochemistry owing to their adjustable components and special interior structure [32–34]. LDHs have the general formula of $[M^{2+}_{1-x}M^{3+}_x(OH)_2]^{x+}(A^{n-})_{x/m}\bullet\ nH_2O$, where the tunable M^{2+} and M^{3+} cations are occupied in the brucite-like layers with a uniform and well-ordered state, and A^{n-} represents the interlayer anions to compensate for the positively charged LDHs. In consideration of the double metal cations composition as well as the unique layered structure, LDHs can be a superior precursor to prepare binary metal sulfides.

In this study, a binary metal sulfide was synthesized using LDH as a starting material and was investigated, for the first time, as a cathode material of AIBs. Control experiments showed that binary metal sulfides is superior to monotypic metal sulfides in the cathodic performance of AIBs. Introduction of reduced graphene oxide (rGO) further improves the performance of binary metal sulfides. This performance-enhancing effect and relating energy storage mechanism will be investigated intensively in this work.

2. Experimental section

2.1. Materials preparation

2.1.1. Preparation of graphene oxide (GO)

GO was prepared according to the modified Hummer's method [35,36]. 360 mL concentrated H_2SO_4 and 40 mL H_3PO_4 was poured into beaker successively, and stirred for 10 min. 3.0 g graphite and 18.0 g potassium permanganate was then added slowly to the mixture, generating a slightly exothermic reaction at 35–40 °C. The reacting mixture was then raised to 50 °C and stirred for 12 h. After cooled to room temperature, the mixture was then poured onto 400 mL of frozen deionized water with 3 mL of 30 wt% hydrogen peroxide and stirred for 30 min. The resulting mixture was centrifuged at 7000 rpm for 10 min to get the solid. The as-obtained solid was washed thoroughly in succession with deionized water, 30 wt% hydrochloric acid and ethanol. The resulting solid was dried under vacuum at 25 °C to obtain GO.

2.1.2. Preparation of NiCo-LDH/rGO

In a typical synthesis, 2.1 mmol of $Ni(NO_3)_2\cdot 6H_2O$, 1.4 mmol $Co(NO_3)_2\cdot 6H_2O$, 0.5 g of hexadecyl trimethyl ammonium bromide (CTAB) and 10 mg of graphite oxide were dissolved in the mixed solution of 60 mL methanol and 12 g deionized water by magnetic stirring. The mixed solution was then transferred to a Teflon-lined autoclave, followed by solvothermal treatment at 180 °C for 24 h. After cooling down to the room temperature naturally, the obtained precipitate was washed with deionized water and ethanol for several times and dried in an oven at 60 °C overnight. For comparison, pure NiCo-LDH was synthesized in the same way at the absence of GO.

2.1.3. Preparation of sulfidized NiCo-LDH/rGO

100 mg of the above NiCo-LDH/rGO and 200 mg sulfur were put into two quartz boats, respectively, and transferred to a tube furnace. The sample was maintained at 300 °C for 2 h to produce sulfur vapor prior to further calcination at 450 °C for 2 h using a ramping rate of 5 °C min^{-1} under the atmosphere of argon. The product was denoted as S–NiCo/rGO.

2.1.4. Preparation of ionic liquid electrolyte

A room temperature ionic liquid electrolyte was made by mixing 1-ethyl-3-methylimidazolium chloride ([EMIm]Cl) and anhydrous aluminum chloride ($AlCl_3$) in an argon-atmosphere glovebox ([O_2] < 0.1 ppm, [H_2O < 0.1 ppm]). The [EMIm]Cl was first baked at 60 °C under vacuum for 10 h to remove residual water, then $AlCl_3$ was gradually dissolved in [EMIm]Cl to form a light yellow transparent solution with a mole ratio of 1.3:1. The electrolyte was standing for at least 12 h prior to use.

2.2. Material characterizations

The crystal structures were characterized by X-ray diffraction (XRD, X'pert PRO MPD with Cu Kα radiation, λ = 1.5406) at a range of 5°-75°. The morphologies and microstructures of the as-obtained materials were observed by scanning electron microscopy (SEM, S-4800 Hitachi) and transmission electron microscopy (TEM, JEM-2100 JEOL). X-ray photoelectron spectroscopy (XPS, PHI 5000 Versa Probe, ULVAC-PHI, Japan) with an Al Kα X-ray source (1486.6 eV) was used to characterize the surface properties of the samples. The nitrogen adsorption-desorption isotherm was collected on a Micrometrics ASAP 2020 analyzer. The sample was degassed at 300 °C for 6 h prior to N_2 sorption. The specific surface areas and pore-size distributions were calculated by the Brunauer-Emmett-Teller (BET) and the Barret-Joyner-Halenda (BJH) method using desorption branch, respectively.

2.3. Electrochemical measurements

The electrochemical measurements were conducted in Swaglok AIB using metallic aluminum foil as an anode. The active materials (S–NiCo/rGO composite) was ground with acetylene black and polyvinylidene difluoride binder at a mass ratio of 6:3:1 in *N*-methyl-2-pyrrolidinone, resulting in a slurry. The cathode was fabricated by coating the slurry onto a rounded Mo (molybdenum) current collector and then dried at 70 °C in a vacuum oven for 12 h. The electrolyte used for the aluminum battery was the mixture of [EMIm]Cl and $AlCl_3$ with a mole ratio of 1:1.3. A single Whatman glass fiber filter (GF/D) was utilized as a separator.

Cyclic voltammogram (CV) measurements were tested at 10 mV s^{-1} over the range of 0.1–2.3 V versus Al/$AlCl_4^-$ on an electrochemical station (CHI 600E, Shanghai China). The capacities and cycling properties of the samples were determined in the potential range from 0.1 to 2.1 V vs Al/$AlCl_4^-$ at different current densities using a multichannel battery tester (LAND-CT2001A). The battery was also analyzed by electrochemical impedance spectroscopy (EIS) in the frequency range of 100 KHz to 100 mHz.

3. Results and discussion

To compare the differences of monotypic and binary sulfides, NiCo, NiAl and CoAl-LDH precursors were first synthesized, and followed by sulfidation to obtain S–NiCo, S–NiAl and S–CoAl. Note that trivalent Al (in its highest valent state) is electrochemically inactive element in AIB system [37,38], therefore S–NiAl and S–CoAl could be regarded as monotypic sulfides. The XRD patterns and SEM morphology of LDHs are presented in Fig. 1ab and

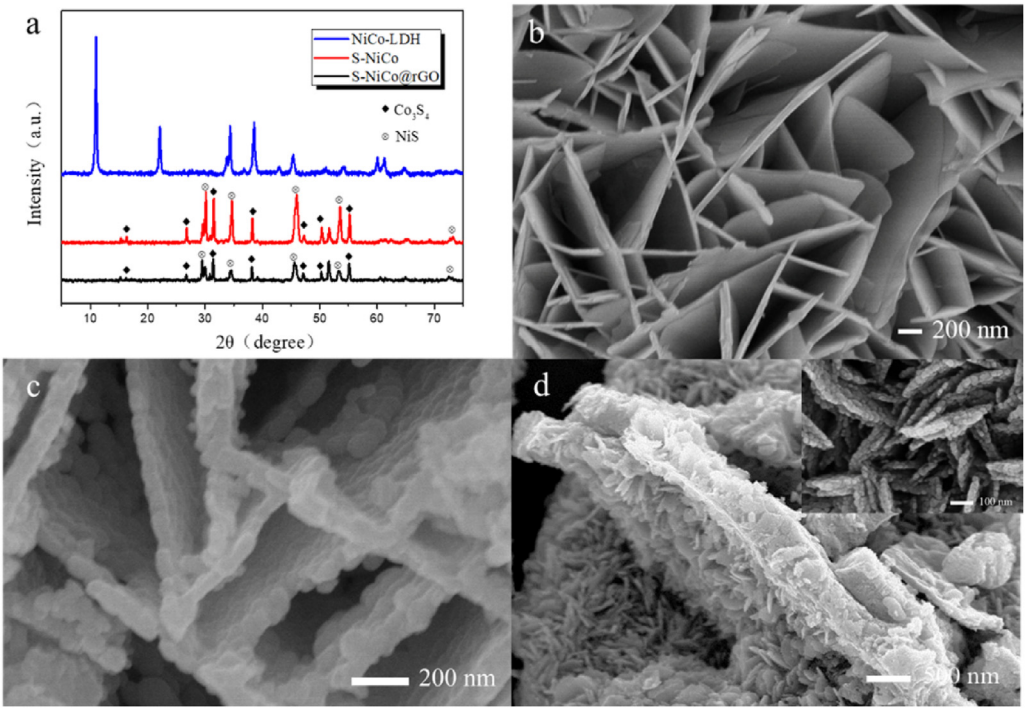

Fig. 1. (a) XRD patterns of NiCo-LDH, S—NiCo and S—NiCo@rGO, SEM images of (b) NiCo-LDH, (c) S—NiCo and (d) S—NiCo@rGO

Figure S1-2. It can be seen that all the three samples presented characteristic peaks of hydrotalcite-like LDH phase and lamellar morphologies, demonstrating the successful preparation of LDH precursors. Fig. 1b presents the morphology of NiCo-LDH precursor, which displays an intercrossed nanowall network. The thickness of the nanosheets are tens of nanometers.

After sulfidation at 450 °C, S—NiCo, S—NiAl and S—CoAl basically maintained the morphology of LDH precursors (Fig. 1c and Figure S3), while the surfaces of the nanosheets become rough, indicating the generation of sulfides. XRD analyses (Fig. 1a and Figure S4) further confirm the transformation from the original hydrotalcite phase for NiAl-LDH and CoAl-LDH to NiS (JCPDS 03-065-3419) and Co_3S_4 (JCPDS 01-073-1703) phases, respectively, after sulfurization. As for NiCo-LDH, a binary nickel-cobalt sulfide was formed after the sulfurization. Besides, the SEM images of S—NiCo obtained at different sulfidation temperatures (300 and 600 °C) are shown in Figure S5. When the temperature decreases to 300 °C, partial LDH sheets are not vulcanized (Figure. S5a), indicating that 300 °C was not high enough to convert hydroxides into sulfides. When the temperature of sulfidation increases to 600 °C, the layered structure of LDH is completely absent (Figure S5b). The sample presents a particle-like morphology, indicating that the lamellar structure of LDH have been completely destroyed at 600 °C. Therefore, the optimized sulfidation temperature is 450 °C.

Galvanostatic charging-discharging test was performed to investigate the electrochemical properties of sulfide samples (Figure S6). As is shown, S—NiCo, S—NiAl and S—CoAl exhibited similar charge and discharge curves at a current density of 1000 mA g^{-1}, and they presented little difference in the initial discharge capacities, which are 158.4, 157.9 and 151 mA h g^{-1}, respectively. However, the cycling performances are obviously different for these three samples. As displayed in Figure S7, after 100 charge and discharge cycles, the discharge capacities of S—NiAl and S—CoAl decreased to 18.9 and 11.7 mAh g^{-1}, respectively, while the discharge capacity of S—NiCo could still remain 42.4 mAh g^{-1}. The better performance of S—NiCo may be due to the lack of inactive Al^{3+} in the sample. It is thought that the presence of inactive Al species may retard the active Ni or Co ions from participating in electrochemical redox reactions in the following cycles.

On account of the better electrochemical performance of S—NiCo, we further combined S—NiCo and rGO to synthesize S—NiCo@rGO. Its synthetic strategy is schematically presented in Scheme 1. NiCo-LDH nanosheets were growing in situ on the surface of rGO, producing a kind of hierarchical structure. Subsequently, the as-obtained NiCo@rGO was vulcanized with sulfur powder at 450 °C in an argon atmosphere to produce S—NiCo@rGO. The S—NiCo@rGO has the similar but weak diffraction peaks to S—NiCo sample (Fig. 1a), demonstrating that the presence of GO does not affect the evolution of crystal phase, but leads to the decrease in the crystal size of NiS and Co_3S_4. Besides, in this sample, the S—NiCo component still maintains the original nanosheet morphology, while the size becomes much smaller due to the presence of GO in the synthesis (Fig. 1d inset).

To investigate potential application of S—NiCo@rGO in AIBs, we employed this sample as a cathode material in an AIB cell. The electrochemical properties of the samples were investigated by CV tests between 0.10 and 2.30 V (vs. $Al/AlCl_4^-$) at the scan rate of 5 mV s^{-1}. As can be seen from Fig. 2a, there are no obvious peaks observed when using bare molybdenum foil, indicating side reactions incurred by Mo foil can be neglected. By contrast, as for S—NiCo and S—NiCo/rGO samples, there are two obvious oxidation peaks located at about 1.1 V, 1.7 V with two reduction peaks located at about 0.9 V and 1.6 V, indicating two different redox reactions are involved in this process. If the cathode potential is high than 2.1 V, the response current increases sharply due to the decomposition of electrolyte. So, the up-limit potential used for galvanostatic charge/discharge is set to be 2.1 V. Fig. 2b shows the initial charge and discharge curves of samples between 0.10 and 2.10 V (vs. $Al/AlCl_4^-$) at the specific current density of 1000 mA g^{-1}. Apparently, there is a long and smooth voltage plateau (~2.0 V vs $Al/AlCl_4^-$) for S—NiCo and S—NiCo/rGO in the initial charge process, which could be

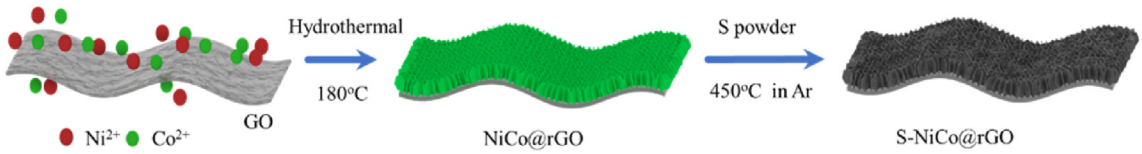

Scheme 1. Schematic illustration of the preparation procedures for the S–NiCo@rGO sample.

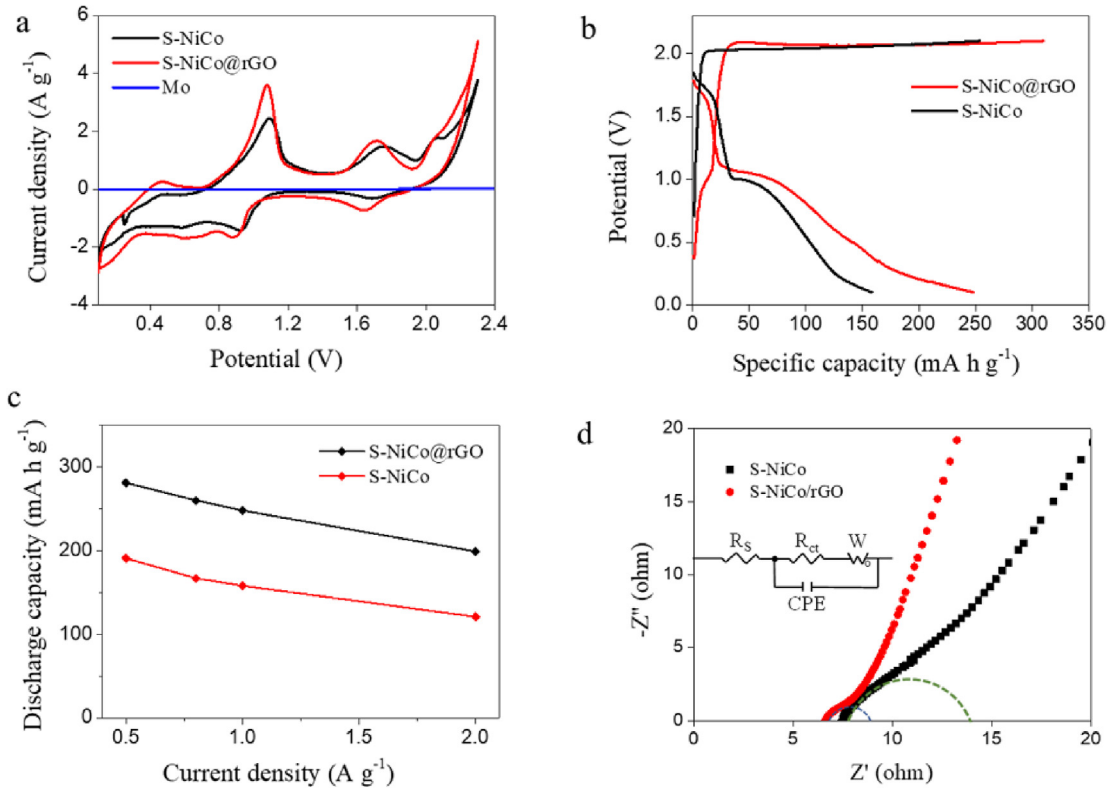

Fig. 2. (a) Typical CV curves of S–NiCo and S–NiCo@rGO at a scan rate of 5 mV s^{-1}, (b) initial charge and discharge curves of S–NiCo and S–NiCo@rGO at a current density of 1000 mA g^{-1}, (c) rate capability of S–NiCo and S–NiCo@rGO at the current density of 0.5–2 A g^{-1}, (d) EIS spectra of S–NiCo and S–NiCo@rGO electrodes.

relevant to the irreversible oxidation of S^{2-} [24] and chlorine generation due to the decomposition of the ionic liquid electrolyte [38]. In addition, the initial discharge curve has two discharge plateaus (~1.6 V and 0.9 V vs $Al/AlCl_4^{-1}$), which coincide with the cathodic peaks in the cyclic voltammogram (Fig. 2a). The discharge capacity of S–NiCo@rGO can reach 248 mAh g^{-1}, which is apparently higher than that of S–NiCo, 158 mAh g^{-1}. This remarkable capacity improvement could be ascribed to the favourable electrical conductivity as well as the larger surface area of S–NiCo/rGO (95 m^2/g of NiCo/rGO vs. 66 m^2/g of S–NiCo, calculated based on N_2 sorption isotherm shown in Figure S8), which are supposed to effectively facilitate electron conduction and exposure of active sites.

The discharge capacities at the current density ranging from 0.5 to 2 A g^{-1} were depicted in Fig. 2c. As can be seen that, at a relative higher current density of 2 A g^{-1}, the discharge capacities of S–NiCo/rGO and S–NiCo are 199 and 121 mAh g^{-1}, respectively, with capacity retention ratio of 70.9% and 62.9% (relevant to their initial capacities at 0.5 A g^{-1}). This indicates that the S–NiCo/rGO has better rate capability than S–NiCo mainly due to the presence of GO.

The electrochemical impedance spectroscopy (EIS) measurements were adopted to analyze the resistances of the electrodes. It is known that the intercept of EIS curve with the X axis denotes the ohmic resistance (Rs), and that the semicircle at high frequencies is related to charge-transfer resistance (R_{ct}). As shown in Fig. 2c, the ohmic resistance of S–NiCo/rGO is smaller than that of S–NiCo, confirming that S–NiCo/rGO has higher electrical conductivity. The charge transfer resistance of S–NiCo@rGO is much smaller than that of S–NiCo, indicating that the presence of rGO can effectually reduce the charge transfer resistance of cathodic redox reactions. The smaller ohmic and charge transfer resistances of S–NiCo/rGO can account for its better rate capability than S–NiCo.

To confirm the feasibility of reversible aluminum ion insertion and extraction behaviors, cyclic voltammogram (CV) curves of S–NiCo/rGO at various scan rates were recorded and shown in Fig. 3a. Clearly, two pairs of reversible redox peaks are observed in each CV curve and the increasing scan rates lead to the increasing peak currents. The relationship of scan rates and peak currents (the inset of Fig. 3a) can reflect the kinetics of the electrode processes. It is obviously that there is a linear relationship between the cathode/anode peak currents and the square root of scan rates, indicating that the aluminum-ion de/intercalation process is controlled by the solid state diffusion of aluminum ion in the host material.

Fig. 3b shows the charge and discharge curves of different cycles for S–NiCo@rGO with cutoff voltage of 0.1 V, which can retain 145,

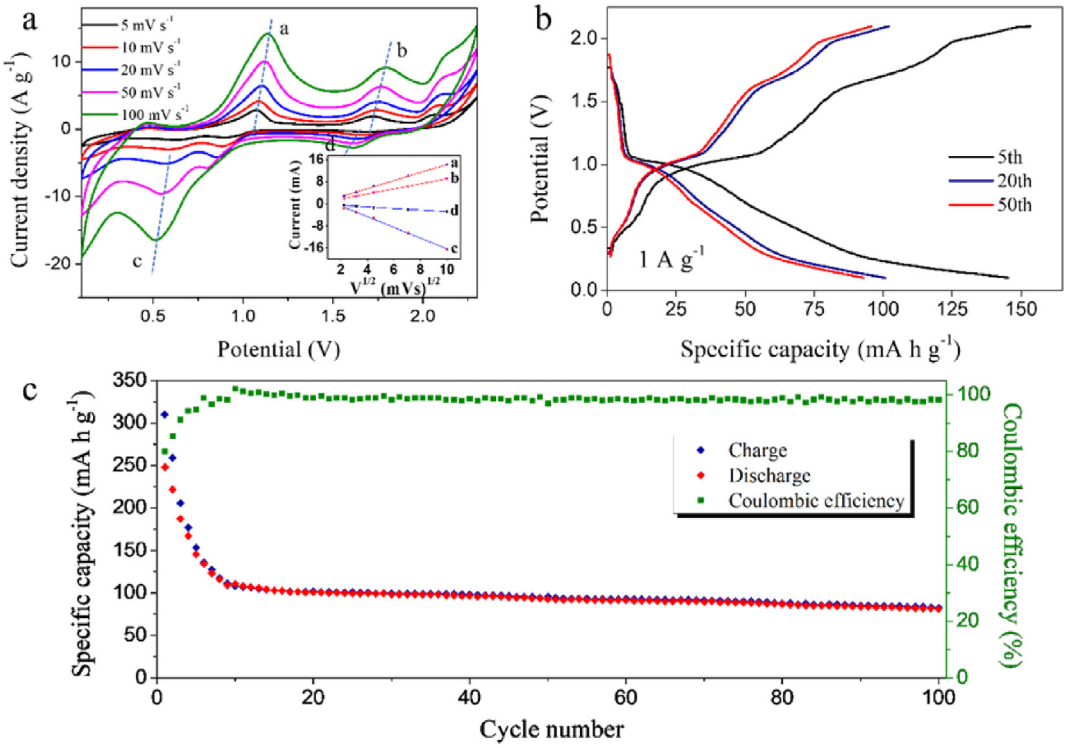

Fig. 3. (a) CV curves at various scan rates from 5 to 100 mV s^{-1}, the inset shows the relation between the currents and the scan rates. (b) The charge and discharge curves of 5th, 20th and 50th cycles of S—NiCo@rGO at a current density of 1000 mA g^{-1}, (c) the cycle performance of S—NiCo@rGO at a current density of 1000 mA g^{-1}.

101, and 93 mA h g^{-1} after 5th, 20th and 50th cycles, respectively. Although it is not unusual to discharge a AIBs cell to a low voltage such as 0.1 V, it would be of more practical significance to set a higher cutoff voltage such as 0.5v [23]. After 100 cycles at the current density of 1000 mA g^{-1} (Fig. 3c), S—NiCo@rGO retains a relatively high capacity of 83 mAh g^{-1} with the coulombic efficiency nearly 100%, indicating a highly reversible electrochemical process during cycling. This performance is one of the best among the metal sulfides reported previously [21–25]. By contrast, the S—NiCo sample can retain only 42.4 mA h g^{-1}, exhibiting much poorer cycle stability (Figure S7). It is worth noting that the rapid capacity decay in the initial ten cycles is always observed for metal oxide and metal sulfide cathode materials of AIBs. The possible reasons for the rapid capacity decay could be attributed to the following two irreversible reactions: (i) the irreversible oxidation of S^{2-}; (ii) decomposition of the electrolyte with the gradual formation of SEI film.

Based on the above experimental data, the improved electrochemical performance of this S—NiCo@rGO composite cathode can be tentatively ascribed to the following points: (i) rGO served as a three-dimensional interconnected conductive network, facilitating the collection and transportation of electrons and therefore decreasing the charge-transfer resistance during cycling; (ii) the rGO could act as a supporting framework, increasing the structural stability of S—NiCo@rGO and hindering S—NiCo pulverization upon repeated cycles; (iii) small size and thickness of S—NiCo in the S—NiCo@rGO can provide more active sites and better tolerate the lattice stress during repeated charge/discharge process, resulting in larger capacity and better cyclic performance. (iv) The smaller size and thickness of S—NiCo in the S—NiCo@rGO makes the ion diffusion distance much shorter and improve the rate performance.

To further explore the energy storage mechanism, X-ray photoelectron spectroscopy (XPS) was conducted to investigate the change of valent state of elements in the electrode at different charging and discharging states. The Al 2p spectra and Cl 2p spectra at different charge/discharge states in the first cycle are displayed in Fig. 4a and b. It is shown that the intensity of Al 2p peak is more intense in the discharged state than that in the charged state. By contrast, the intensities of Cl 2p peaks are similar whenever in the charged or the discharged states. This indicates that the intercalating/de-intercalating ions may be Al^{3+}, rather than $AlCl_4^-$. These Cl elements are thought to be from some irreversible reactions [39]. S 2p spectra of the pristine, fully charged and fully discharged states in the first cycle are depicted in Figure S9. It can be seen that the pristine S 2p spectrum consists of two major peaks at 162.8 eV and 161.7 eV, which are assigned to the S $2p_{3/2}$ and S $2p_{1/2}$. Moreover, the peak at around 168.5 is attributed to the sulfur at a higher oxidation state, which comes from the oxidation of S^{2-} in the atmosphere. When the electrode was charged to 2.1 V versus $Al/AlCl_4^-$, the peak of S around 168.5 eV shifts to 169.4 eV, which is caused by the oxidation of sulfur$^-$ under a high potential during the charging process. This result manifests that the long and smooth voltage plateau in the initial charge at about 2.0 V versus $Al/AlCl_4^-$ could be associated with the oxidation of sulfur, and this is consistent with the previous report [23]. Fig. 4c–d displayed the Ni 2p spectra of S—NiCo/rGO after the first fully charge and discharge. In Fig. 4c, it can be seen that the Ni 2p spectra has two dominant peaks at 873.7 and 856.1 eV, which correspond to the binding energies of Ni $2p_{1/2}$ and Ni $2p_{3/2}$, respectively. When the electrode was fully discharged to 0.1 V, two new peaks appear at around 852.4 and 869.6 eV, which can be ascribed to Ni^0. The similar phenomenon also can be found in the spectra of Co 2p. As is shown in Fig. 4e, at the fully charged state, the Co 2p spectra of S—NiCo-rGO consists of two spin-orbit doublets at 780.0 and 796.0 eV that are assigned to Co^{2+}, while the other two peaks at 781.8 and 797.5 eV are ascribed to Co^{3+}. When the electrode was fully discharged to

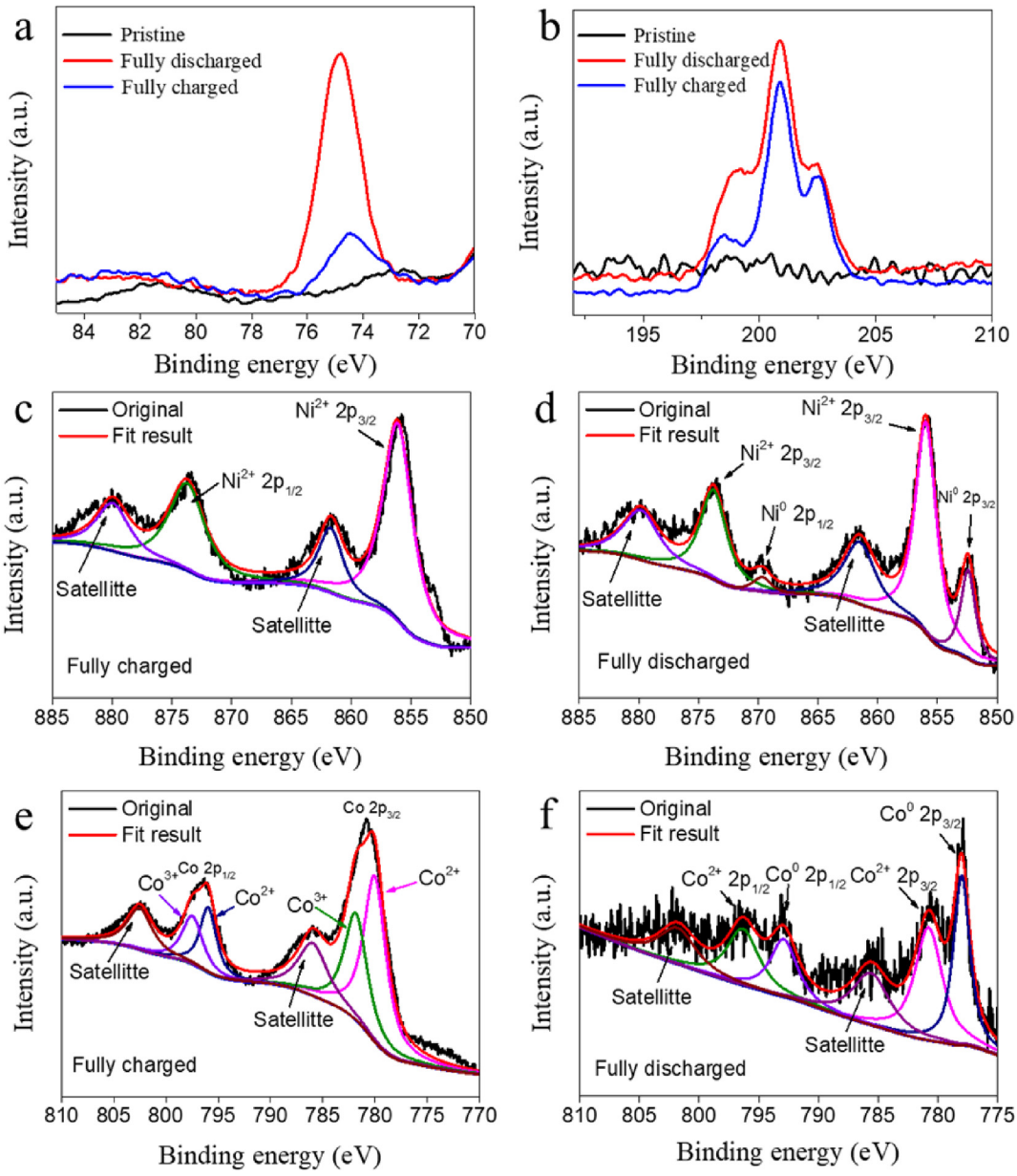

Fig. 4. Ex situ XPS spectra of S–NiCo@rGO at different charge/discharge states. (a) Al and (b) Cl 2p at pristine, first fully charged and fully discharged states. Ni 2p spectra at the first fully charged (c) and discharged states (d). Co 2p spectra at the first fully charged (e) and discharged (f) states.

0.1 V, two new intense peaks emerged at 778.2 and 793.2 eV (Fig. 4f), which are the characteristic peaks of Co^0. On the basis of the changes in valence, it can be deduced that the substitution of Ni^{2+} and Co^{2+}/Co^{3+} with Al^{3+} occurred as a result of the incorporation of Al^{3+} into the electrode (specifically, NiS and Co_3S_4 phase) during the discharging process. To confirm this deduction, ex-situ XRD measurements were carried out. All the electrodes were sealed with polyimide (PI) film during the XRD measurements to avoid any contact with air and moisture. As shown in Figure S10, the diffraction peak of molybdenum foil at 40.52° was taken as a reference peak for correction. After the initial discharge, the diffraction peak at 45.72°, which corresponds to (102) plane of NiS, shifts slightly to 45.70°, as a result of partial substitution of Ni^{2+} with smaller Al^{3+}. Besides, this diffraction peak shifted back to 45.72° at the fully charged state. The similar situation was found for the diffraction peak at 37.5° which corresponds to (400) plane of Co_3S_4. This reversible changes in crystal structure demonstrate again that the intercalating ion is Al^{3+} cation, rather than large-sized $AlCl_4^-$, during the discharge process, since the incorporation of $AlCl_4^-$ could lead to significant changes of crystal structure for the electrode material. This mechanism is similar to that observed for the $CoSe_2$ based cathode material in our previous work [39]. Based on the discussion above, the reaction mechanism of S–NiCo@rGO during charge-discharge could be described as follows:

In the discharge process,

$$4Al_2Cl_7^- \rightarrow 7AlCl_4^- + Al^{3+} \quad (1)$$

$$NiS + mAl^{3+} + 3me^- \rightarrow Al_mNi_nS + (1 - n)Ni \quad (2)$$

$$Co_3S_4 + pAl^{3+} + 3pe^- \rightarrow Al_pCo_qS_4 + (3 - q)Co \quad (3)$$

In the charge process,

$$7AlCl_4^- + Al^{3+} \rightarrow 4Al_2Cl_7^- \quad (4)$$

$$Al_mNi_nS + (1 - n)Ni - 3me^- \rightarrow NiS + mAl^{3+} \quad (5)$$

$$Al_pCo_qS_4 + (3 - q)Co - 3pe^- \rightarrow Co_3S_4 + pAl^{3+} \quad (6)$$

4. Conclusion

In conclusion, a S−NiCo@rGO composite material has been fabricated by a facile hydrothermal reaction followed by a sulfidation treatment. The resulting S−NiCo@rGO electrode exhibits excellent performance when applied as a cathode material for AIBs. The initial discharge capacity of S−NiCo@rGO reaches 248 mA h g^{-1} at the current density of 1000 mA g^{-1}, and maintains a reversible discharge capacity of 83 mA h g^{-1} after 100 cycles with the coulombic efficiency of nearly 100%. The charge storage mechanism of this material is found to be due to the substitution of Ni^{2+} and Co^{2+}/Co^{3+} by Al^{3+}. This work highlights the promising prospect of developing high performance AIBs using LDH-derived cathode materials.

Declaration of competing interest

The authors declare that they have no known competing financial interests or personal relationships that could have appeared to influence the work reported in this paper.

CRediT authorship contribution statement

Wei Xing: Conceptualization, Methodology, Funding acquisition. **Xiaochen Li:** Data curation, Writing - original draft. **Tonghui Cai:** Data curation, Writing - original draft. **Yu Zhang:** Visualization, Investigation. **Peng Bai:** Visualization, Investigation. **Jing Xu:** Visualization, Investigation. **Han Hu:** Validation. **Mingbo Wu:** Validation. **Qingzhong Xue:** Visualization, Investigation, Validation. **Yi Zhao:** Investigation. **Jin Zhou:** Investigation. **Shuping Zhuo:** Investigation. **Xiuli Gao:** Conceptualization, Methodology, Funding acquisition. **Zifeng Yan:** Writing - review & editing.

Acknowledgements

This work was financially supported by National Natural Science Foundation of China (51877216), Taishan Scholar Foundation (tsqn20161017), Major Program of Shandong Province Natural Science Foundation (ZR201801280009), and Fundamental Research Funds for the Central Universities (18CX05007A, 19CX05001A, 19CX05002A).

Appendix A. Supplementary data

Supplementary data to this article can be found online at https://doi.org/10.1016/j.electacta.2020.136174.

References

[1] P.K. Nayak, L.T. Yang, W. Brehm, P. Adelhelm, From lithium-ion to sodium-ion batteries: advantages, challenges, and surprises, Angew. Chem. Int. Ed. 57 (2018) 102−120.
[2] Y.X. Huang, L.Z. Zhao, L. Li, M. Xie, F. Wu, R.J. Chen, Electrolytes and electrolyte/electrode interfaces in sodium-ion batteries: from scientific research to practical application, Adv. Mater. 31 (2019) 1808393.
[3] Z. Ali, M. Asif, X.X. Huang, T.Y. Tang, Y.L. Hou, Hierarchically porous Fe_2CoSe_4 binary-metal selenide for extraordinary rate performance and durable anode of sodium-ion batteries, Adv. Mater. 30 (2018) 1802745.
[4] Y.N. Xu, X.W. Deng, Q.D. Li, G.B. Zhang, F.Y. Xiong, S.S. Tan, Q.L. Wei, J. Lu, J.T. Li, Q.Y. An, L.Q. Mai, Vanadium oxide pillared by interlayer Mg^{2+} ions and water as ultralong-life cathodes for magnesium-ion batteries, Inside Chem. 5 (2019) 1194−1209.
[5] Y.H. Tan, W.T. Yao, T.W. Zhang, T. Ma, L.L. Lu, F. Zhou, H.B. Yao, S.H. Yu, High voltage magnesium-ion battery enabled by nanocluster Mg_3Bi_2 alloy anode in noncorrosive electrolyte, ACS Nano 12 (2018) 5856−5865.
[6] D.M. Kim, S.C. Jung, S. Ha, Y. Kim, Y. Park, J.H. Ryu, Y.K. Han, K.T. Lee, Cointercalation of Mg^{2+} ions into graphite for magnesium-ion batteries, Chem. Mater. 30 (2018) 3199−3203.
[7] M. Walter, K.V. Kravchyk, C. Bofer, R. Widmer, M.V. Kovalenko, Poly pyrenes as high-performance cathode materials for aluminum batteries, Adv. Mater. 30 (2018) 1705644.
[8] D.J. Kim, D.J. Yoo, M.T. Otley, A. Prokofjevs, C. Pezzato, M. Owczarek, S.J. Lee, J.W. Choi, J.F. Stoddart, Rechargeable aluminium organic batteries, Nature Energ 4 (2019) 51−59.
[9] Y. Zhang, S.Q. Liu, Y.J. Ji, J.M. Ma, H.J. Yu, Emerging nonaqueous aluminum-ion batteries: challenges, status, and perspectives, Adv. Mater. 30 (2018) 1706310.
[10] K. Liang, L.C. Ju, S. Koul, A. Kushima, Y. Yang, Self-supported tin sulfide porous films for flexible aluminum-ion batteries, Adv. Energ. Mater. 9 (2019) 1802543.
[11] X.Z. Yu, B. Wang, D.C. Gong, Z. Xu, B.G. Lu, Graphene nanoribbons on highly porous 3d graphene for high-capacity and ultrastable Al-ion batteries, Adv. Mater. 29 (2017) 1604118.
[12] S. Liu, J.J. Hu, N.F. Yan, G.L. Pan, G.R. Li, X.P. Gao, Aluminum storage behavior of anatase TiO_2 nanotube arrays in aqueous solution for aluminum ion batteries, Energy Environ. Sci. 5 (2012) 9743−9746.
[13] Y.Y. Liu, S.B. Sang, Q.M. Wu, Z.G. Lu, K.Y. Liu, H.T. Liu, The electrochemical behavior of Cl- assisted Al^{3+} insertion into titanium dioxide nanotube arrays in aqueous solution for aluminum ion batteries, Electrochim. Acta 143 (2014) 340−346.
[14] J.R. Gonzalez, F. Nacimiento, M. Cabello, R. Alcantara, P. Lavela, J.L. Tirado, Reversible intercalation of aluminium into vanadium pentoxide xerogel for aqueous rechargeable batteries, RSC Adv. 6 (2016) 62157−62164.
[15] M.C. Lin, M. Gong, B.G. Lu, Y.P. Wu, D.Y. Wang, M.Y. Guan, M. Angell, C.X. Chen, J. Yang, B.J. Hwang, H.J. Dai, An ultrafast rechargeable aluminium-ion battery, Nature 520 (2015) 324−328.
[16] Y.P. Wu, M. Gong, M.C. Lin, C.Z. Yuan, M. Angell, L. Huang, D.Y. Wang, X.D. Zhang, J. Yang, B.J. Hwang, H.J. Dai, 3D graphitic foams derived from chloroaluminate anion intercalation for ultrafast aluminum-ion battery, Adv. Mater. 28 (2016) 9218−9222.
[17] D.Y. Wang, C.Y. Wei, M.C. Lin, C.J. Pan, H.L. Chou, H.A. Chen, M. Gong, Y.P. Wu, C.Z. Yuan, M. Angell, Y.J. Hsieh, Y.H. Chen, C.Y. Wen, C.W. Chen, B.J. Hwang, C.C. Chen, H.J. Dai, Advanced rechargeable aluminium ion battery with a high-quality natural graphite cathode, Nat. Commun. 8 (2017) 14283.
[18] S.K. Das, Graphene: a cathode material of choice for aluminum-ion batteries, Angew. Chem. Int. Ed. 57 (2018) 16606−16617.
[19] L.Y. Zhang, L. Chen, H. Luo, X.F. Zhou, Z.P. Liu, Large-sized few-layer graphene enables an ultrafast and long-life aluminum-ion battery, Adv. Energ. Mater. 7 (2017) 1700034.
[20] H. Chen, F. Guo, Y.J. Liu, T.Q. Huang, B.N. Zheng, N. Ananth, Z. Xu, W.W. Gao, C. Gao, A defect-free principle for advanced graphene cathode of aluminum-ion battery, Adv. Mater. 29 (2017) 1605958.
[21] Y.X. Hu, D.L. Ye, B. Luo, H. Hu, X.B. Zhu, S.C. Wang, L.L. Li, S.J. Peng, L.Z. Wang, A binder-free and free-standing cobalt sulfide@carbon nanotube cathode material for aluminum-ion batteries, Adv. Mater. 30 (2018) 1703824.
[22] Y.X. Hu, B. Luo, D.L. Ye, X.B. Zhu, M.Q. Lyu, L.Z. Wang, An innovative freeze-dried reduced graphene oxide supported SnS_2 cathode active material for aluminum-ion batteries, Adv. Mater. 29 (2017) 1606132.
[23] S. Wang, Z.J. Yu, J.G. Tu, J.X. Wang, D.H. Tian, Y.J. Liu, S.Q. Jiao, A novel aluminum-ion battery: Al/$AlCl_3$-[EMIm]Cl/Ni_3S_2@Graphene, Adv. Energ. Mater. 6 (2016) 1600137.
[24] L.X. Geng, J.P. Scheifers, C.Y. Fu, J. Zahang, B.P.T. Fokwa, J.C. Guo, Titanium sulfides as intercalation-type cathode materials for rechargeable aluminum batteries, ACS Appl. Mater. Interfaces 9 (2017) 21251−21257.
[25] L.X. Geng, G.C. Lv, X.B. Xing, J.C. Guo, Reversible electrochemical intercalation of aluminum in Mo_6S_8, Chem. Mater. 27 (2015) 4926−4929.
[26] X.Y. Yu, X.W. Lou, Mixed metal sulfides for electrochemical energy storage and conversion, Adv. Energ. Mater. 8 (2018) 1701592.
[27] P. Kulkarni, S.K. Nataraj, R.G. Balakrishna, D.H. Nagaraju, M.V. Reddy, Nanostructured binary and ternary metal sulfides: synthesis methods and their application in energy conversion and storage devices, J. Mater. Chem. 5 (2017) 22040−22094.
[28] W.Y. Li, B.J. Zhang, R.J. Lin, S. Ho-Kimura, G.J. He, X.Y. Zhou, J.Q. Hu, I.P. Parkin, A dendritic nickel cobalt sulfide nanostructure for alkaline battery electrodes, Adv. Funct. Mater. 28 (2018) 1705937.
[29] G.J. He, M. Qiao, W.Y. Li, Y. Lu, T.T. Zhao, R.J. Zou, B. Li, J.A. Darr, J.Q. Hu, M.M. Titirici, I.P. Parkin, S, N-co-doped graphene-nickel cobalt sulfide aerogel: improved energy storage and electrocatalytic performance, Adv. Sci. 4 (2017) 1600214.
[30] C.Y. Zhang, X.Y. Cai, Y. Qian, H.F. Jiang, L.J. Zhou, B.S. Li, L.F. Lai, Z.X. Shen, W. Huang, Electrochemically synthesis of nickel cobalt sulfide for high-performance flexible asymmetric supercapacitors, Adv. Sci. 5 (2018) 1700375.

[31] Y. Liu, Z.B. Wang, Y.J. Zhong, M. Tade, W. Zhou, Z.P. Shao, Molecular design of mesoporous $NiCo_2O_4$ and $NiCo_2S_4$ with sub-micrometer-polyhedron architectures for efficient pseudocapacitive energy storage, Adv. Funct. Mater. 27 (2017) 1701229.
[32] X.J. Li, M.Y. Xin, S. Guo, T.H. Cai, D.F. Du, W. Xing, L.M. Zhao, W.Y. Guo, Q.Z. Xue, Z.F. Yan, Insight of synergistic effect of different active metal ions in layered double hydroxides on their electrochemical behaviors, Electrochim. Acta 253 (2017) 302–310.
[33] X.J. Li, J. Zhou, X.C. Li, M.Y. Xin, T.H. Cai, W. Xing, Y.M. Chai, Q.Z. Xue, Z.F. Yan, Bifunctional petaloid nickel manganese layered double hydroxides decorated on a freestanding carbon foam for flexible asymmetric supercapacitor and oxygen evolution, Electrochim. Acta 252 (2017) 275–285.
[34] X.J. Li, D.F. Du, Y. Zhang, W. Xing, Q.Z. Xue, Z.F. Yan, Layered double hydroxides toward high-performance supercapacitors, J. Mater. Chem. 5 (2017) 15460–15485.
[35] W.S.H. Jr, R.E. Offeman, Preparation of graphitic oxide, J. Am. Chem. Soc. 80 (1958), 1339-1339.
[36] D.C. Marcano, D.V. Kosynkin, J.M. Berlin, A. Sinitskii, Z.Z. Sun, A. Slesarev, L.B. Alemany, W. Lu, J.M. Tour, Improved synthesis of graphene oxide, ACS Nano 4 (2010) 4806–4814.
[37] X.F. Zhang, G.H. Zhang, S. Wang, S.J. Li, S.Q. Jiao, Porous CuO microsphere architectures as high-performance cathode materials for aluminum-ion batteries, J. Mater. Chem. 6 (2018) 3084–3090.
[38] J. Shi, J. Zhang, J. Guo, Avoiding pitfalls in rechargeable aluminum batteries research, ACS Energy Lett 4 (2019) 2124–2129.
[39] T. Cai, L. Zhao, H. Hu, T. Li, X. Li, S. Guo, Y. Li, Q. Xue, W. Xing, Z. Yan, L. Wang, Stable $CoSe_2$/carbon nanodevice@reduced graphene oxide composites for high-performance rechargeable aluminum-ion batteries, Energy Environ. Sci. 11 (2018) 2341–2347.